Letter

Multiple topological phases in tetradymite compounds M_2Te_2P (M = Ti, Zr, or Hf)

M. J. Pan,[1,2,*] B.-X. Li,[1,2,*] H. Wang,[3,4,*] J. D. Liu,[1,2] F. M. Chen,[1,2] J. R. Huang,[1,2] G. X. Qu,[1,2] S. Y. Gao,[1,2] B. Jiang,[1,2] Y.-B. Huang,[5] X. Shi,[6] T.-L. Xia,[3,4,7,8,†] H. M. Weng,[1,2,9,‡] and T. Qian[1,§]

[1]*Beijing National Laboratory for Condensed Matter Physics and Institute of Physics, Chinese Academy of Sciences, Beijing 100190, China*

[2]*University of Chinese Academy of Sciences, Beijing 100049, China*

[3]*Department of Physics, Renmin University of China, Beijing 100872, China*

[4]*Beijing Key Laboratory of Opto-electronic Functional Materials and Micro-nano Devices, Renmin University of China, Beijing 100872, China*

[5]*Shanghai Synchrotron Radiation Facility, Shanghai Advanced Research Institute, Chinese Academy of Sciences, Shanghai 201204, China*

[6]*Centre for Quantum Physics, Key Laboratory of Advanced Optoelectronic Quantum Architecture and Measurement (MOE), School of Physics, Beijing Institute of Technology, Beijing 100081, China*

[7]*Key Laboratory of Quantum State Construction and Manipulation (Ministry of Education), Renmin University of China, Beijing 100872, China*

[8]*Laboratory for Neutron Scattering, Renmin University of China, Beijing 100872, China*

[9]*Songshan Lake Materials Laboratory, Dongguan 523808, China*

(Received 22 December 2023; revised 25 April 2024; accepted 22 May 2024; published 4 June 2024)

Since the advent of time-reversal-invariant topological insulators, the generalization of topology concepts has led to the discovery of a wide range of topological states. These topological states may undergo topological phase transitions (TPTs) accompanied by discontinuous changes in topological invariants. In this Letter, by combining time- and angle-resolved photoemission spectroscopy measurements with first-principles calculations, we have demonstrated the existence of distinct TPTs in the unoccupied states above the Fermi level in the M_2Te_2P (M = Ti, Zr, or Hf) family. These TPTs arise from the inversion of the transition metal d and Te p orbitals due to the enhancement of spin-orbit coupling and variation in crystal fields, as the transition metal changes from 3d to 4d and then to 5d. Eventually, dual topological states are achieved in the 5d system Hf_2Te_2P, where a type-III Dirac semimetal state coexists with a strong topological insulator state. Finally, we reveal a rapid relaxation process in the nonequilibrium population of the Dirac surface state due to the presence of an additional interband scattering channel in the bulk.

DOI: 10.1103/PhysRevB.109.L220102

Topological insulators represent a class of novel states of quantum matter characterized by gapless boundary states traversing the bulk band gap, protected by nontrivial topology within the bulk [1–11]. They are categorized based on topological invariants, such as strong and weak topological insulators distinguished by the Z_2 topological invariant [5]. Another important class of topological states, topological semimetals, feature protected band crossings between valence and conduction bands, categorized by the number and dimensionality of band degeneracy, such as Dirac and Weyl semimetals with four- and twofold degenerate points, respectively [12–24]. The degenerate points with a nonzero Chern number exhibit exotic surface Fermi arcs connecting their surface projections [12]. Topological phase transitions (TPTs) may occur between different types of topological states by varying various parameters, such as spin-orbit coupling (SOC) strength, lattice constants, time-reversal symmetry, and crystalline symmetries, as observed in $ZrTe_5$ [25–27], $TlBi(S_{1-x}Se_x)_2$ [28,29], and EuB_6 [30–32]. TPTs could lead to substantial changes in topological effects, offering potential applications in topological electronic devices. Furthermore, multiple topological states can coexist in a single material. For instance, previous studies have identified both topological insulator and Dirac semimetal (DSM) states in the iron-based superconductors Li(Fe,Co)As [33], and both three-component fermions and two-component Weyl fermions in MoP [21]. The coexistence of multiple topological states provides a platform to study the interplay between topological quantum phenomena.

Tetradymite structural compounds, exemplified by Bi_2Se_3, have garnered significant attention due to their remarkable topological properties [9–11], where the introduction of transition metals has led to the emergence of intriguing topological effects, such as the quantum anomalous Hall effect [34,35]. First-principles calculations have predicted that the involvement of transition metal d orbitals can lead to rich topological properties in the M_2Te_2P (M = Ti, Zr, or Hf) family of tetradymite structure [36–39]. Angle-resolved photoemission spectroscopy (ARPES) measurements have revealed unusual surface Dirac node arcs with nontrivial spin

*These authors contributed equally to this work.
†Corresponding author: tlxia@ruc.edu.cn
‡Corresponding author: hmweng@iphy.ac.cn
§Corresponding author: tqian@iphy.ac.cn

textures in all compounds of this family [37–42]. However, many crucial topological characteristics reside in the unoccupied states above the Fermi level (E_F) and cannot be accessed with conventional ARPES experimental techniques.

In this Letter, we have conducted a comprehensive exploration of the topological properties in the unoccupied states of M_2Te_2P (M = Ti, Zr, or Hf) using time-resolved ARPES (tr-ARPES) combined with first-principles calculations. Our findings provide direct evidence for the existence of TPTs resulting from the inversion of the transition metal d and Te p orbitals due to the enhancement of SOC and variation in crystal fields. Remarkably, we unveil a type-III DSM state coexisting with a strong topological insulator (STI) state in Hf_2Te_2P, in which the Dirac point (DP) is composed of a flat band and a dispersive band. In addition, the nonequilibrium population of the Dirac surface state exhibits a rapid decay towards the equilibrium state, distinct from the behavior in the well-known STI Bi_2Se_3.

High-quality single crystals of M_2Te_2P were synthesized using the chemical vapor transport method [36,43]. Sample surfaces for ARPES measurements were obtained by *in situ* cleavage under ultrahigh vacuum conditions. The tr-ARPES experiments were performed at the Institute of Physics, Chinese Academy of Sciences, using pump laser pulses of 1.2/2.4 eV and probe laser pulses of 6/7.2 eV at a repetition rate of 500 kHz [44]. We used a configuration with an energy resolution of 10 meV and a time resolution of ~300 fs for unoccupied state measurements. For dynamic measurements, we used a configuration with an energy resolution of 30 meV and a time resolution of ~100 fs. Synchrotron ARPES experiments were performed at the "Dreamline" beamline of the Shanghai Synchrotron Radiation Facility. All ARPES data were taken at 10 K. First-principles calculations were performed using a plane-wave basis set and the projector augmented-wave method [45], implemented in the Vienna *ab initio* simulation package [46,47] for electronic structure calculations. The exchange-correlation functional employed was the generalized gradient approximation with the pseudopotential parametrized by Perdew, Burke, and Ernzerhof [48]. Slab calculations were performed using the WANNIER90 [49,50] software to construct a tight-binding model that fits with the band structure obtained from the first-principles calculation software VASP. Fermi surfaces (FSs) were computed using the open-source code WANNIERTOOLS [51] with the iterative Green's function method.

We take Zr_2Te_2P as an example to illustrate the crystal structure and electronic structure of the M_2Te_2P family in Fig. 1. Figure 1(a) shows that Zr_2Te_2P has a layered crystal structure, consisting of quintuple layers stacked via van der Waals forces. Each quintuple layer has a stacking sequence of Te-Zr-P-Zr-Te atomic layers. Because of weak interlayer coupling, the electronic structure exhibits a quasi-two-dimensional character. In Fig. 1(c), the FSs are composed of large elliptical electronlike pockets centered at the Brillouin zone (BZ) boundary and small circular holelike pockets surrounding the BZ center. Figure 1(d) exhibits that although there are no global band gaps in the electronic structure of Zr_2Te_2P, direct gaps exist throughout the BZ when considering SOC. We focus on the topological properties of two direct gaps, Δ1 and Δ2, as indicated in Fig. 1(d). The slab

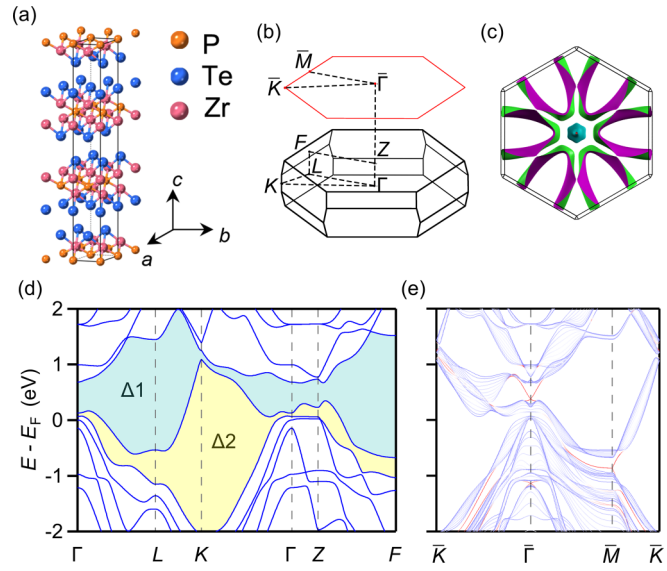

FIG. 1. (a) Crystal structure of Zr_2Te_2P with black lines indicating the conventional unit cell. (b) Bulk and (001) surface BZs. (c) Calculated FSs of Zr_2Te_2P. (d) Calculated bulk band structure of Zr_2Te_2P along high-symmetry lines with SOC. Light blue and yellow regions represent the continuous band gaps Δ1 and Δ2, respectively. (e) Calculated band structure along high-symmetry lines of a slab of ten quintuple layers of Zr_2Te_2P. Red and blue lines represent surface and bulk bands, respectively.

calculations in Fig. 1(e) reveal the presence of Dirac-like surface states at the time-reversal-invariant momenta (TRIM) $\bar{\Gamma}$ and $\bar{M}$ in the two gaps, indicating nontrivial topological properties. The surface bands within Δ2 are almost degenerate along $\bar{\Gamma}$-$\bar{M}$, resulting in surface Dirac node arcs, which have been observed in previous ARPES experiments [37–42]. The surface Dirac cone at the $\bar{\Gamma}$ point within Δ1 lies above E_F and awaits experimental confirmation.

We investigate the changes in the topological properties upon replacing the transition metal in the M_2Te_2P family. Since the crystal structure possesses inversion symmetry, Z_2 topological invariants can be derived by analyzing the parity eigenvalues of all occupied bands at eight TRIM, namely, Γ, Z, three L, and three F points [5]. The calculated parity eigenvalues for Δ1 and Δ2 are listed in Table I. For Δ1, the Z_2 topological invariant $(\nu_0;\nu_1\nu_2\nu_3)$ in Ti_2Te_2P is $(0;000)$, signifying its trivial topological property. In contrast, Δ1 has a strong topological invariant $\nu_0 = 1$ in Zr_2Te_2P and Hf_2Te_2P. In the case of Δ2, it has a strong topological invariant $\nu_0 = 1$ in Ti_2Te_2P and Zr_2Te_2P. A previous study suggested that Δ2 has a weak topological invariant in Hf_2Te_2P based on parity analysis at the TRIM [39]. However, our band calculations

TABLE I. Parity products of all occupied bands for Δ1 and Δ2 at eight TRIM in Ti_2Te_2P, Zr_2Te_2P, and Hf_2Te_2P.

Sample	Γ	Z	$3F$	$3L$	(Δ1)	Γ	Z	$3F$	$3L$	(Δ2)
Ti_2Te_2P	−	+	−	+	Trivial	−	−	−	+	STI
Zr_2Te_2P	−	−	−	+	STI	−	−	−	+	STI
Hf_2Te_2P	−	−	−	+	STI			No gap		

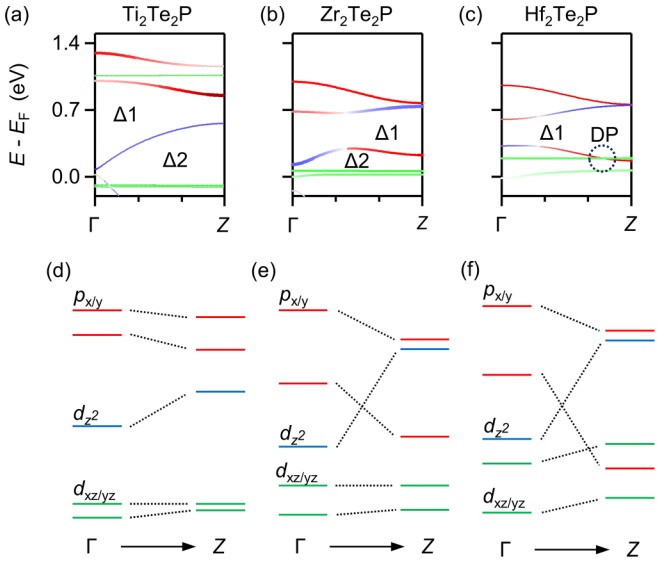

FIG. 2. (a)–(c) Calculated bulk bands along Γ-Z with SOC for (a) Ti_2Te_2P, (b) Zr_2Te_2P, and (c) Hf_2Te_2P. Red, blue, and green colors represent the components of the $p_{x/y}$, d_{z^2}, and $d_{xz/yz}$ orbitals, respectively. The dashed circle in (c) indicates the DP on Γ-Z. (d)–(f) Schematic plots of band inversion along Γ-Z for (d) Ti_2Te_2P, (e) Zr_2Te_2P, and (f) Hf_2Te_2P.

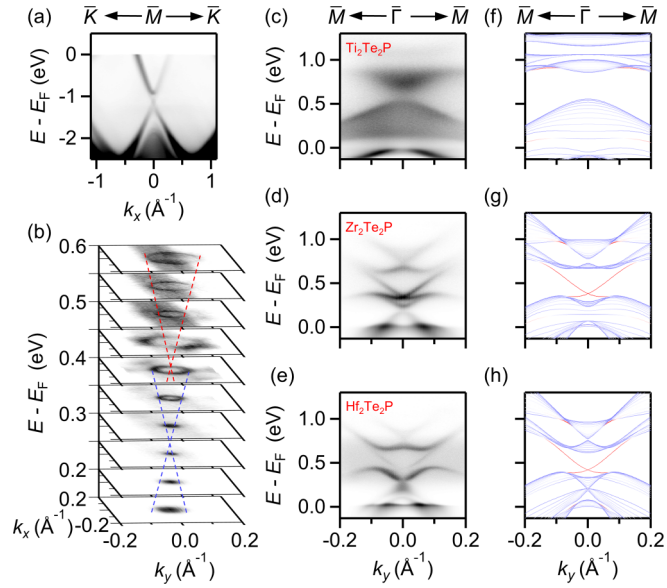

FIG. 3. (a) ARPES intensity plot along $\bar{M}$-$\bar{K}$ for Hf_2Te_2P. The data were collected with synchrotron light at a photon energy of 94 eV. (b) Stacking intensity plot of tr-ARPES data at different constant energies above E_F for Hf_2Te_2P, showing the coexistence of the DSM state and Dirac surface state. Red and blue lines are guides to the eye that indicate the band dispersions of surface and bulk Dirac cones, respectively. (c)–(e) The tr-ARPES intensity plots along $\bar{\Gamma}$-$\bar{M}$ of (c)Ti_2Te_2P, (d) Zr_2Te_2P, and (e) Hf_2Te_2P at zero delay time. The data in (b), (d), and (e) were collected with a 2.4-eV pump and 6-eV probe, and in (c) were collected with a 2.4-eV pump and 7.2-eV probe because the results obtained with the 6-eV probe include not only the unoccupied states but also image potential state (Fig. S4 in the Supplemental Material [52]). (f)–(h) Calculated band structures along $\bar{\Gamma}$-$\bar{M}$ of a slab of ten quintuple layers of (f) Ti_2Te_2P, (g) Zr_2Te_2P, and (h) Hf_2Te_2P. Red and black lines represent surface and bulk bands, respectively.

reveal that Δ2 is closed in Hf_2Te_2P due to the presence of a band crossing along Γ-Z [Fig. 2(c)], rendering the parity analysis no longer applicable. The band crossing results in a DSM state in Hf_2Te_2P. The parity analysis and band calculations demonstrate the existence of TPTs in both Δ1 and Δ2 of the M_2Te_2P family.

To elucidate the origin of the TPTs, we analyze the evolution in the band structure along Γ-Z upon replacing the transition metal in Fig. 2. The related bands are dominantly formed by the Te $p_{x/y}$ and transition metal d_{z^2} and $d_{xz/yz}$ orbitals, represented by red, blue, and green colors, respectively. Figures 2(a) and 2(d) show that there is no band inversion along Γ-Z in Δ1 for Ti_2Te_2P, consistent with its trivial topological property. In Figs. 2(b) and 2(c), the $p_{x/y}$ bands shift downward due to the variation in crystal fields associated with an increase in lattice constants in Zr_2Te_2P and Hf_2Te_2P. Consequently, a band inversion occurs between the lower $p_{x/y}$ band and the d_{z^2} band along Γ-Z, resulting in a TPT from a trivial insulator state to a STI state in Δ1. This TPT is manifested by the appearance of a surface Dirac cone at the $\bar{\Gamma}$ point within Δ1 in the slab calculations (Fig. S1 in Supplemental Material [52]).

While the parity analysis reveals a strong topological invariant $\nu_0 = 1$ for Δ2 in Ti_2Te_2P and Zr_2Te_2P, there is no band inversion along Γ-Z in Δ2 in Figs. 2(a) and 2(b). The STI property of Δ2 originates from the band inversion at the L point, manifested by the Dirac surface state at the $\bar{M}$ point (Fig. S1 in Supplemental Material [52]). Figure 2(c) shows that the enhancement of SOC in the 5d orbitals increases the splitting of the $d_{xz/yz}$ bands, resulting in an upward shift of the upper $d_{xz/yz}$ band. Consequently, a band inversion occurs between the upper $d_{xz/yz}$ band and the lower $p_{x/y}$ band along Γ-Z in Hf_2Te_2P. Since the two bands on Γ-Z belong to different irreducible representations under $\hat{C}_3$ rotation symmetry, the hybridization between them is avoided, forming a DP, as indicated in Fig. 2(c). This results in a TPT from a STI state to a DSM state in Δ2. We note that the DP is composed of a dispersive band and an extremely flat band along Γ-Z. It is referred to as type-III DP, representing the critical state at the Lifshitz transition between type-I and type-II DPs. The type-III DP serves as the contact point between linelike electron and hole FSs along Γ-Z. The distinctive linelike FSs are protected by a nontrivial topological invariant and can lead to unique physical properties, such as a critical chiral magnetoresponse [22].

The calculations indicate that while the topological characteristics in Δ1 and Δ2 are distributed in both occupied and unoccupied states, the TPTs originates from the band inversions along Γ-Z in the unoccupied states above E_F. In Fig. 3(a), the band dispersions of Hf_2Te_2P measured with synchrotron light exhibit a Dirac surface state at the $\bar{M}$ point within Δ2 below E_F, in agreement with previous ARPES results and band calculations [36–42]. The Dirac surface state is observed in all compounds of the M_2Te_2P family, in agreement with the slab calculations (Figs. S1 and S2 in Supplemental Material [52]), demonstrating that the band inversion at the L point remains unchanged with element

substitution. However, the synchrotron ARPES data do not provide any evidence of the TPTs, since the band inversions are expected to occur in the unoccupied states above E_F. Therefore, we employed time-resolved ARPES with the pump-probe method to investigate the theoretically proposed TPTs.

Figures 3(c)–3(e) display band dispersions along $\bar{\Gamma}$-$\bar{M}$ in the unoccupied states of M_2Te_2P (M = Ti, Zr, or Hf). In Fig. 3(c), the ARPES data for Ti_2Te_2P reveal two gaps located around 0.6 and 0.05 eV above E_F, corresponding to $\Delta 1$ and $\Delta 2$, respectively. The gap size of $\Delta 1$ at the $\bar{\Gamma}$ point being 240 meV (Fig. S3 in Supplemental Material [52]). The broad distribution of spectral intensity above E_F is attributed to the surface projection of the bulk band continuum with finite k_z dispersions. We mention that the samples are of high quality since our synchrotron ARPES data show clear band dispersions below E_F for Ti_2Te_2P (Fig. S2 in Supplemental Material [52]). Despite a minor discrepancy with the calculations in gap size, the experimental and calculated topological properties agree. No Dirac surface state is observed within $\Delta 1$ of Ti_2Te_2P, consistent with its trivial topological property. In contrast, the ARPES data for Zr_2Te_2P and Hf_2Te_2P in Figs. 3(d) and 3(e) distinctly exhibit a surface Dirac cone at the $\bar{\Gamma}$ point within $\Delta 1$, in agreement with the slab calculations in Figs. 3(g) and 3(h). These findings provide direct evidence of the TPT from a trivial insulator state to a STI state in $\Delta 1$.

We proceed to examine the TPT in $\Delta 2$. Compared to Ti_2Te_2P, $\Delta 2$ in Zr_2Te_2P is narrowed and shifts upward to around 0.2 eV above E_F in Fig. 3(d). No Dirac surface state is observed at the $\bar{\Gamma}$ point within $\Delta 2$ for both Ti_2Te_2P and Zr_2Te_2P in Figs. 3(c) and 3(d). Given the presence of one surface Dirac cone at the $\bar{M}$ point (Fig. S2 in Supplemental Material [52]), there are a total of three surface Dirac cones within $\Delta 2$ in the whole surface BZ, manifesting the STI property of $\Delta 2$ in Ti_2Te_2P and Zr_2Te_2P. In the case of Hf_2Te_2P, the ARPES data in Fig. 3(e) reveal that $\Delta 2$ is closed, forming a gapless Dirac cone located around 0.3 eV above E_F at the $\bar{\Gamma}$ point. This observation agrees well with the slab calculations showing a bulk Dirac cone in Fig. 3(h), except for a slight underestimation of the energy position of the DP in the calculations. This Dirac cone exhibits a broad distribution of spectral intensity, in contrast to the Dirac surface state with well-defined band dispersions in $\Delta 1$ in Fig. 3(e). Therefore, the Dirac cone around 0.3 eV above E_F is attributed to the surface projection of the bulk band continuum with finite k_z dispersions. The observation of a bulk Dirac cone demonstrates the TPT from a STI state to a DSM state in $\Delta 2$. In Fig. 3(b), the three-dimensional plot of the tr-ARPES data above E_F illustrates the coexistence of surface and bulk Dirac cones at the $\bar{\Gamma}$ point in Hf_2Te_2P. As the calculations show that the type-III DP is composed of a dispersive band and a flat band along Γ-Z, its projection along the [001] direction results in an almost isotropic Dirac cone in agreement with the experimental results. In addition, unusual surface Dirac node arcs have been observed along $\bar{\Gamma}$-$\bar{M}$ [37–42]. These results indicate that Hf_2Te_2P exhibits rich and exotic topological properties.

We further investigate the dynamic process of the nonequilibrium state above E_F, using Zr_2Te_2P as an example because the dynamical properties exhibited by the other materials are

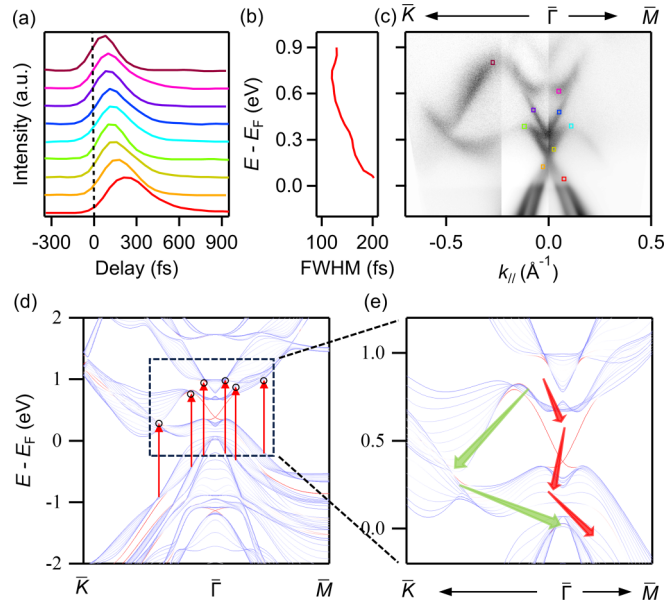

FIG. 4. (a) Delay time dependence of tr-ARPES spectral intensity of Zr_2Te_2P, whose energy and momentum positions are indicated in (c). The data were collected using 1.2-eV pump and 6-eV probe with an improved time resolution of ~100 fs. (b) The curve depicting full width at half maximum (FWHM) values in (a) with respect to energy level. (c) The tr-ARPES intensity plot along $\bar{K}$-$\bar{\Gamma}$-$\bar{M}$ of Zr_2Te_2P at zero delay time, collected with a 1.2-eV pump and 7.2-eV probe. (d) Accessible channels for optical excitation under a 1.2-eV pump are indicated by red arrows in the slab calculations of Zr_2Te_2P. (e) Schematic representation for the relaxation process of photoexcited electrons back to the equilibrium state via electron-electron scattering. Red and green arrows indicate bulk-to-bulk and bulk-to-surface interband scattering channels, respectively.

nearly identical. Figure 4(a) shows the variation of spectral intensity with delay time at different energy-momentum positions of the unoccupied state. The relaxation curves of high-lying states exhibit a Gauss-like shape with its width close to the time resolution, indicating a rapid decay towards the equilibrium state. Figure 4(b) exhibits that the relaxation time moderately increases at lower-energy positions. The relaxation process remains consistently rapid whether for surface or bulk states in Zr_2Te_2P, in contrast to the long-lived population of the Dirac surface state observed in the well-known STI Bi_2Se_3 [53–56]. The large bulk band gap in Bi_2Se_3 renders electron-phonon coupling incapable of recombining electrons with the valence bands, leading to a metastable population at the bulk conduction band edge, which feeds a nonequilibrium population of the surface state persisting for >10 ps [54]. Our tr-ARPES data with a larger momentum range along $\bar{\Gamma}$-$\bar{K}$ in Fig. 4(c) reveal a band overlap in Zr_2Te_2P, caused by the projection along k_z of the bulk bands, as shown in the slab calculations in Fig. 4(e). Figure 4(d) illustrates that direct optical excitation by a 1.2-eV pump results in a nonequilibrium population of high-lying states in the bulk. After excitation, electrons relax back to the occupied state through intra- and interband scattering. As illustrated in Fig. 4(e), unlike in Bi_2Se_3 [54], the Dirac surface state is not the only channel in the relaxation process in Zr_2Te_2P, since

the band overlap provides an additional interband scattering channel in the bulk. Therefore, although the topological surface state observed in $\Delta 1$ closely resembles that in Bi_2Se_3, the additional scattering channel leads to distinct behavior in the relaxation process.

In summary, we have clearly revealed the existence of multiple topological states in the M_2Te_2P family. The transition metal d orbitals play a crucial role in these topological states. As the transition metal changes from $3d$ to $4d$ and then to $5d$, the d-p type band inversions occur successively, resulting in distinct TPTs in different bulk band gaps. The band inversion in Hf_2Te_2P results in a type-III DP composed of a flat band and a dispersive band. This marks the identification of a topological semimetal state in tetradymite structural compounds, where many well-known topological insulators have been discovered. The coexistence of type-III DPs with surface Dirac nodal arcs and an almost isotropic surface Dirac cone in a single topological material provides a promising platform for studying the interplay between different types of Dirac fermions at different locations in energy-momentum space.

This work was supported by the Ministry of Science and Technology of China (Grants No. 2022YFA1403800 and No. 2019YFA0308602), the National Natural Science Foundation of China (Grants No. U22A6005, No. 11925408, No. 11921004, No. 12188101, No. 12074425, No. 11874422, and No. 12204042), the Chinese Academy of Sciences (Grant No. XDB33000000), the Informatization Plan of Chinese Academy of Sciences (Grant No. CAS-WX2021SF-0102), the Synergetic Extreme Condition User Facility (SECUF), and the "Dreamline" beamline of Shanghai Synchrotron Radiation Facility (SSRF).

[1] C. L. Kane and E. J. Mele, Phys. Rev. Lett. **95**, 226801 (2005).
[2] C. L. Kane and E. J. Mele, Phys. Rev. Lett. **95**, 146802 (2005).
[3] B. A. Bernevig and S.-C. Zhang, Phys. Rev. Lett. **96**, 106802 (2006).
[4] B. A. Bernevig, T. L. Hughes, and S.-C. Zhang, Science **314**, 1757 (2006).
[5] L. Fu and C. L. Kane, Phys. Rev. B **76**, 045302 (2007).
[6] L. Fu, C. L. Kane, and E. J. Mele, Phys. Rev. Lett. **98**, 106803 (2007).
[7] X. Dai, T. L. Hughes, X.-L. Qi, Z. Fang, and S.-C. Zhang, Phys. Rev. B **77**, 125319 (2008).
[8] D. Hsieh, D. Qian, L. Wray, Y. Xia, Y. S. Hor, R. J. Cava, and M. Z. Hasan, Nature (London) **452**, 970 (2008).
[9] H. Zhang, C.-X. Liu, X.-L. Qi, X. Dai, Z. Fang, and S.-C. Zhang, Nat. Phys. **5**, 438 (2009).
[10] Y. Xia, D. Qian, D. Hsieh, L. Wray, A. Pal, H. Lin, A. Bansil, D. Grauer, Y. S. Hor, R. J. Cava *et al.*, Nat. Phys. **5**, 398 (2009).
[11] Y. Chen, J.-H. Chu, J. Analytis, Z. Liu, K. Igarashi, H.-H. Kuo, X. Qi, S.-K. Mo, R. Moore, D. Lu *et al.*, Science **329**, 659 (2010).
[12] X. Wan, A. M. Turner, A. Vishwanath, and S. Y. Savrasov, Phys. Rev. B **83**, 205101 (2011).
[13] G. Xu, H. Weng, Z. Wang, X. Dai, and Z. Fang, Phys. Rev. Lett. **107**, 186806 (2011).
[14] Z. Wang, Y. Sun, X.-Q. Chen, C. Franchini, G. Xu, H. Weng, X. Dai, and Z. Fang, Phys. Rev. B **85**, 195320 (2012).
[15] Z. Liu, B. Zhou, Y. Zhang, Z. Wang, H. Weng, D. Prabhakaran, S.-K. Mo, Z. Shen, Z. Fang, X. Dai *et al.*, Science **343**, 864 (2014).
[16] H. Weng, C. Fang, Z. Fang, B. A. Bernevig, and X. Dai, Phys. Rev. X **5**, 011029 (2015).
[17] B. Q. Lv, H. M. Weng, B. B. Fu, X. P. Wang, H. Miao, J. Ma, P. Richard, X. C. Huang, L. X. Zhao, G. F. Chen, Z. Fang, X. Dai, T. Qian, and H. Ding, Phys. Rev. X **5**, 031013 (2015).
[18] S.-Y. Xu, I. Belopolski, N. Alidoust, M. Neupane, G. Bian, C. Zhang, R. Sankar, G. Chang, Z. Yuan, C.-C. Lee *et al.*, Science **349**, 613 (2015).
[19] A. A. Soluyanov, D. Gresch, Z. Wang, Q. Wu, M. Troyer, X. Dai, and B. A. Bernevig, Nature (London) **527**, 495 (2015).
[20] B. Bradlyn, J. Cano, Z. Wang, M. Vergniory, C. Felser, R. J. Cava, and B. A. Bernevig, Science **353**, aaf5037 (2016).
[21] B. Lv, Z.-L. Feng, Q.-N. Xu, X. Gao, J.-Z. Ma, L.-Y. Kong, P. Richard, Y.-B. Huang, V. Strocov, C. Fang *et al.*, Nature (London) **546**, 627 (2017).
[22] H. Huang, K.-H. Jin, and F. Liu, Phys. Rev. B **98**, 121110(R) (2018).
[23] Z. Rao, H. Li, T. Zhang, S. Tian, C. Li, B. Fu, C. Tang, L. Wang, Z. Li, W. Fan *et al.*, Nature (London) **567**, 496 (2019).
[24] B. Q. Lv, T. Qian, and H. Ding, Rev. Mod. Phys. **93**, 025002 (2021).
[25] H. Weng, X. Dai, and Z. Fang, Phys. Rev. X **4**, 011002 (2014).
[26] C. Vaswani, L.-L. Wang, D. H. Mudiyanselage, Q. Li, P. M. Lozano, G. D. Gu, D. Cheng, B. Song, L. Luo, R. H. J. Kim, C. Huang, Z. Liu, M. Mootz, I. E. Perakis, Y. Yao, K. M. Ho, and J. Wang, Phys. Rev. X **10**, 021013 (2020).
[27] P. Zhang, R. Noguchi, K. Kuroda, C. Lin, K. Kawaguchi, K. Yaji, A. Harasawa, M. Lippmaa, S. Nie, H. Weng *et al.*, Nat. Commun. **12**, 406 (2021).
[28] S.-Y. Xu, Y. Xia, L. Wray, S. Jia, F. Meier, J. Dil, J. Osterwalder, B. Slomski, A. Bansil, H. Lin *et al.*, Science **332**, 560 (2011).
[29] T. Sato, K. Segawa, K. Kosaka, S. Souma, K. Nakayama, K. Eto, T. Minami, Y. Ando, and T. Takahashi, Nat. Phys. **7**, 840 (2011).
[30] S. Nie, Y. Sun, F. B. Prinz, Z. Wang, H. Weng, Z. Fang, and X. Dai, Phys. Rev. Lett. **124**, 076403 (2020).
[31] S.-Y. Gao, S. Xu, H. Li, C.-J. Yi, S.-M. Nie, Z.-C. Rao, H. Wang, Q.-X. Hu, X.-Z. Chen, W.-H. Fan *et al.*, Phys. Rev. X **11**, 021016 (2021).
[32] W. L. Liu, X. Zhang, S. M. Nie, Z. T. Liu, X. Y. Sun, H. Y. Wang, J. Y. Ding, Q. Jiang, L. Sun, F. H. Xue, Z. Huang, H. Su, Y. C. Yang, Z. C. Jiang, X. L. Lu, J. Yuan, S. Cho, J. S. Liu, Z. H. Liu, M. Ye *et al.*, Phys. Rev. Lett. **129**, 166402 (2022).
[33] P. Zhang, Z. Wang, X. Wu, K. Yaji, Y. Ishida, Y. Kohama, G. Dai, Y. Sun, C. Bareille, K. Kuroda *et al.*, Nat. Phys. **15**, 41 (2019).
[34] R. Yu, W. Zhang, H.-J. Zhang, S.-C. Zhang, X. Dai, and Z. Fang, Science **329**, 61 (2010).
[35] C.-Z. Chang, J. Zhang, X. Feng, J. Shen, Z. Zhang, M. Guo, K. Li, Y. Ou, P. Wei, L.-L. Wang *et al.*, Science **340**, 167 (2013).

[36] K. Chen, S. Das, D. Rhodes, S. Memaran, T. Besara, T. Siegrist, E. Manousakis, L. Balicas, and R. Baumbach, J. Phys.: Condens. Matter **28**, 14LT01 (2016).
[37] H. Ji, I. Pletikosić, Q. D. Gibson, G. Sahasrabudhe, T. Valla, and R. J. Cava, Phys. Rev. B **93**, 045315 (2016).
[38] K.-W. Chen, N. Aryal, J. Dai, D. Graf, S. Zhang, S. Das, P. Le Fèvre, F. Bertran, R. Yukawa, K. Horiba *et al.*, Phys. Rev. B **97**, 165112 (2018).
[39] M. M. Hosen, K. Dimitri, A. K. Nandy, A. Aperis, R. Sankar, G. Dhakal, P. Maldonado, F. Kabir, C. Sims, F. Chou *et al.*, Nat. Commun. **9**, 3002 (2018).
[40] T. J. Boyle, A. Rossi, M. Walker, P. Carlson, M. K. Miller, J. Zhao, P. Klavins, C. Jozwiak, A. Bostwick, E. Rotenberg, V. Taufour, I. M. Vishik, and E. H. da Silva Neto, Phys. Rev. B **100**, 081105(R) (2019).
[41] J. Dai, E. Frantzeskakis, N. Aryal, K.-W. Chen, F. Fortuna, J. E. Rault, P. Le Fèvre, L. Balicas, K. Miyamoto, T. Okuda, E. Manousakis, R. E. Baumbach, and A. F. Santander-Syro, Phys. Rev. Lett. **126**, 196407 (2021).
[42] G. Dhakal, F. Kabir, A. K. Nandy, A. Aperis, A. P. Sakhya, S. Pradhan, K. Dimitri, C. Sims, S. Regmi, M. M. Hosen *et al.*, Phys. Rev. B **106**, 125124 (2022).
[43] K. Tschulik, M. Ruck, M. Binnewies, E. Milke, S. Hoffmann, W. Schnelle, B. P. Fokwa, M. Gilleßen, and P. Schmidt, Eur. J. Inorg. Chem. **2009**, 3102 (2009).
[44] M. Pan, J. Liu, F. Chen, J. Wang, C. Yun, and T. Qian, Rev. Sci. Instrum. **95**, 013001 (2024).
[45] P. E. Blöchl, Phys. Rev. B **50**, 17953 (1994).
[46] G. Kresse and J. Furthmüller, Phys. Rev. B **54**, 11169 (1996).
[47] G. Kresse and D. Joubert, Phys. Rev. B **59**, 1758 (1999).
[48] J. P. Perdew, K. Burke, and M. Ernzerhof, Phys. Rev. Lett. **77**, 3865 (1996).
[49] A. A. Mostofi, J. R. Yates, Y.-S. Lee, I. Souza, D. Vanderbilt, and N. Marzari, Comput. Phys. Commun. **178**, 685 (2008).
[50] N. Marzari, A. A. Mostofi, J. R. Yates, I. Souza, and D. Vanderbilt, Rev. Mod. Phys. **84**, 1419 (2012).
[51] Q. Wu, S. Zhang, H.-F. Song, M. Troyer, and A. A. Soluyanov, Comput. Phys. Commun. **224**, 405 (2018).
[52] See Supplemental Material at http://link.aps.org/supplemental/10.1103/PhysRevB.109.L220102 for multiple topological phases in tetradymite compounds M_2Te_2P (M = Ti, Zr, or Hf).
[53] A. Sterzi, G. Manzoni, L. Sbuelz, F. Cilento, M. Zacchigna, P. Bugnon, A. Magrez, H. Berger, A. Crepaldi, and F. Parmigiani, Phys. Rev. B **95**, 115431 (2017).
[54] J. A. Sobota, S. Yang, J. G. Analytis, Y. L. Chen, I. R. Fisher, P. S. Kirchmann, and Z.-X. Shen, Phys. Rev. Lett. **108**, 117403 (2012).
[55] Y. H. Wang, D. Hsieh, E. J. Sie, H. Steinberg, D. R. Gardner, Y. S. Lee, P. Jarillo-Herrero, and N. Gedik, Phys. Rev. Lett. **109**, 127401 (2012).
[56] J. Sánchez-Barriga, E. Golias, A. Varykhalov, J. Braun, L. V. Yashina, R. Schumann, J. Minár, H. Ebert, O. Kornilov, and O. Rader, Phys. Rev. B **93**, 155426 (2016).